




## RESEARCH ARTICLE

# High-entropy stabilized oxides derived via a low-temperature template route for high-performance lithium-sulfur batteries

Hassan Raza<sup>1</sup>  | Junye Cheng<sup>2</sup>  | Cong Lin<sup>1</sup>  | Soumyadip Majumder<sup>1</sup> | Guangping Zheng<sup>1</sup> | Guohua Chen<sup>1,3</sup>

<sup>1</sup>Department of Mechanical Engineering, Research Institute for Smart Energy, The Hong Kong Polytechnic University, Hong Kong SAR, P. R. China

<sup>2</sup>Department of Materials Science, Shenzhen MSU-BIT University, Shenzhen, P. R. China

<sup>3</sup>School of Energy and Environment, City University of Hong Kong, Hong Kong SAR, P. R. China

## Correspondence

Junye Cheng, Department of Materials Science, Shenzhen MSU-BIT University, Shenzhen, Guangdong 517182, P. R. China.

Email: [chengjunye@mbu.edu.cn](mailto:chengjunye@mbu.edu.cn)

Guohua Chen, Department of Mechanical Engineering, Research Institute for Smart Energy, The Hong Kong Polytechnic University, Hung Hom, Kowloon, Hong Kong SAR, P. R. China.

Email: [ghchen1963@gmail.com](mailto:ghchen1963@gmail.com)

## Funding information

R&D Projects in Key Areas of Guangdong Province, Grant/Award Number: 2019B090908001; The Guangdong Province Science & Technology Bureau, Grant/Award Number: 2020A0505090011; Guangdong-Hong Kong-Macao Joint Lab for Photonic-Thermal-Electrical Energy Materials and Devices, Grant/Award Number: 2019B121205001; Science, Technology, and Innovation Commission of Shenzhen Municipality, Grant/Award Number: SGDX20190816230615451

## Abstract

It is a long-standing issue that the sluggish polysulfide conversion and adverse shuttling effects impede the development of lithium-sulfur (Li-S) batteries with high energy density and cycling stability, which necessitate the exploration of new electrocatalysts to facilitate the practical applications of Li-S batteries. Herein, a single-phase high-entropy stabilized oxide ( $\text{Ni}_{0.2}\text{Co}_{0.2}\text{Cu}_{0.2}\text{Mg}_{0.2}\text{Zn}_{0.2}\text{O}$ ) (HEO850) is successfully prepared through a novel low-temperature annealing strategy from a self-sacrificing metal-organic frameworks (MOFs) template and then integrated into the sulfur host, where it functions as both the catalytic converter and chemical inhibitor towards the shuttle species. Furthermore, the synergistic contribution of randomly dispersed metal elements and the exposure of affluent active sites enable the chemical encapsulation of soluble polysulfides and accelerate conversion kinetics. The HEO850/S/KB cathode (KB: ketjen black; sulfur content: 70 wt.%) delivers a substantially higher initial specific discharge capacity of  $\sim 1244 \text{ mAh g}^{-1}$  in comparison to MEO/S/KB (MEO: medium entropy oxide;  $\sim 980 \text{ mAh g}^{-1}$ ), LEO/S/KB (LEO: low entropy oxide;  $\sim 908 \text{ mAh g}^{-1}$ ), and routine S/KB cathodes ( $\sim 966 \text{ mAh g}^{-1}$ ), which is well retained at  $\sim 784 \text{ mAh g}^{-1}$  after 800 cycles at 0.5 C with a low capacity decay rate of  $\sim 0.043\%$  per cycle. Moreover, when the HEO850/S/KB cathode is processed with a high areal sulfur loading ( $\sim 4.4 \text{ mg cm}^{-2}$ ), the resulting Li-S battery also performs well, with a high initial specific capacity of  $\sim 1044 \text{ mAh g}^{-1}$  at 0.1 C and 85% capacity retention after 100 cycles. This study highlights the potential application of HEOs in enhancing the performance of Li-S batteries and provides a novel strategy in synthesizing the HEOs at a relatively low annealing temperature for various energy conversion and storage applications.

## KEYWORDS

catalytic conversion, high entropy oxides, lithium-sulfur batteries, multicomponent synergistic effect, multi-metallic MOFs

This is an open access article under the terms of the [Creative Commons Attribution](https://creativecommons.org/licenses/by/4.0/) License, which permits use, distribution and reproduction in any medium, provided the original work is properly cited.

© 2023 The Authors. *EcoMat* published by The Hong Kong Polytechnic University and John Wiley & Sons Australia, Ltd.

## 1 | INTRODUCTION

The high-performance lithium-sulfur (Li-S) batteries have been recognized as the most competitive alternative to the state-of-the-art lithium-ion batteries (LIBs) to meet the ever-increasing demand for the energy-dense and electrochemically sustainable storage devices in the emerging fields, such as flexible and portable electronics, electric vehicles, and smart grids.<sup>1–3</sup> Li-S batteries utilize the naturally abundant, and environmentally benign sulfur as the cathode, possessing an overwhelming theoretical capacity of 1675 mAh g<sup>−1</sup> (more than six times higher than that of conventional LiCoO<sub>2</sub> cathode) and a high energy density of 2600 or 2800 Wh L<sup>−1</sup>.<sup>4,5</sup> However, despite these superiorities in their potential performances, the Li-S batteries still have some challenges before their commercialization, which are rooted from the complex multielectron conversion electrochemical reaction: 16Li + S<sub>8</sub> → 8Li<sub>2</sub>S.<sup>6</sup> Several significant obstacles have been identified: the inferior redox cycling life span, low sulfur utilization on account of the insulating sulfur and lithium sulfides, the sluggish electrochemical kinetics, irreversible sulfur loss, low Coulombic efficiency, as well as the fast capacity fading. The soluble polysulfide intermediates (Li<sub>2</sub>S<sub>x</sub>, 4 ≤ x ≤ 8) in the liquid electrolytes results in the shuttling effect between the cathode and anode which is a typical challenge for Li-S batteries.<sup>7,8</sup>

The functional sulfur hosts have offered tremendous contributions to inhibit the shuttling effect by encapsulating the lithium polysulfides (LiPSs). Initially, this strategy was explored by introducing the porous carbon to retain LiPSs<sup>9–18</sup> physically to remarkably improve the performance of Li-S batteries. However, the volume expansion during the charge/discharge processes limits this physical strategy to only partial confinement of the intermediate polysulfides.<sup>9–13</sup> Because of their strong chemical bonding capability, the polar multicomponent metal oxides additives have recently become effective chemical inhibitors towards the cathode solvated polysulfides.<sup>14–17</sup> For example, the strong chemical bonding between Zn or Co and S in the porous spinel ZnCo<sub>2</sub>O<sub>4</sub> particles@N-doped reduced graphene oxide (ZnCo<sub>2</sub>O<sub>4</sub>@N-RGO) and the dual bonding (Li-O and Sr-S bonds) in the novel Ba<sub>0.5</sub>Sr<sub>0.5</sub>Co<sub>0.8</sub>Fe<sub>0.2</sub>O<sub>3–δ</sub> perovskite nanoparticles have been validated as an efficient chemical anchoring strategy for the LiPSs species,<sup>15,17</sup> which comprise the mixed metal oxides with preferable electronic conductivity and chemical stability as a single entity.<sup>18–20</sup> Given so significant role of the metal species in the mixed metal oxides, it is highly desirable to explore the efficient and characteristic multi-metal oxide catalysts with easily exposed

and well dispersed metal atoms to effectively anchor the polysulfides in Li-S batteries.

High entropy oxides (HEOs) are a class of new crystalline solid solutions articulated by deliberately populating five or more different metals into a single cationic sublattice, making them unique as compared to traditional metal oxides. The configurational entropic contribution to the Gibbs free energy is highlighted in these crystal formulations rather than the cohesive energy.<sup>18</sup> Subsequently, these single-phase multi-metal oxides possess highly randomly dispersed metal sites and outstanding electrochemical features,<sup>21–25</sup> including the reversible Li<sup>+</sup> storage<sup>26</sup> and superior Li<sup>+</sup> conductivity (>10<sup>−3</sup> S cm<sup>−1</sup>).<sup>27</sup> In this regard, a high entropy oxide based on Ni, Mg, Cu, Zn, and Co was synthesized by a mechanochemically assisted method and utilized as the chemical anchor for LiPSs, delivering an initial discharge capacity of ~890 mAh g<sup>−1</sup> and achieving a capacity retention of ~479 mAh g<sup>−1</sup> after 600 cycles because of the synergistic contribution of the Li-O and Ni-S bonding.<sup>46</sup> However, the synthesis techniques including aforementioned route for the single-phase HEOs, such as the nebulized spray pyrolysis (NSP), flame spray pyrolysis (FSP), solid-phase sintering (SPS), and reverse co-precipitation (RCP)<sup>26,28,29</sup> require relatively complex and expensive reaction equipment, high energy consumption, long preparation time, and extremely high annealing temperature (>1000°C), along with relatively large particle sizes of the products.<sup>26,28</sup> Moreover, potential of HEOs as a novel cathode host has not been well studied. For example, alternative synthesis strategy at lower annealing temperature is needed to facilitate the tailoring of HEOs properties with more exposed metal species and active sites for multiple engineering and energy-related applications.

Herein, we developed a novel low-temperature template strategy to prepare the high entropy oxide (Ni<sub>0.2</sub>Co<sub>0.2</sub>Cu<sub>0.2</sub>Mg<sub>0.2</sub>Zn<sub>0.2</sub>)O from a self-sacrificing multi-metal-organic frameworks (M-MOFs). When employed as the cathode component for Li-S batteries, the HEOs can provide many randomly distributed active metal sites with excellent electronic conductivity and multicomponent synergistic effects in anchoring the polysulfides. Thus, it leads to a high initial specific discharge capacity of ~1244 mAh g<sup>−1</sup> at 0.5 C and retains a capacity of ~784 mAh g<sup>−1</sup> even after 800 redox cycles with a low degradation of ~0.043% per cycle. Furthermore, the different entropy stabilized metal oxides (low-entropy and medium-entropy) were compared with HEOs for Li-S performance. Importantly, the underlying mechanisms were investigated by ex-situ X-ray photoelectron spectrometer (XPS) and X-ray diffractometer (XRD).

## 2 | EXPERIMENTAL SECTION

### 2.1 | Syntheses of HEOs

All the materials and chemicals (Section 1.1, supporting information) were used as received. The high entropy oxide,  $(\text{Ni}_{0.2}\text{Co}_{0.2}\text{Cu}_{0.2}\text{Mg}_{0.2}\text{Zn}_{0.2})\text{O}$ , was prepared by low-temperature annealing of a self-sacrificing MOFs template. First, the MOFs template containing the Ni, Co, Cu, Mg, and Zn was synthesized by the one-pot solvothermal method. In detail, 4.4 mg of each metal nitrate (i.e.,  $\text{Ni}(\text{NO}_3)_2 \cdot 6\text{H}_2\text{O}$ ,  $\text{Co}(\text{NO}_3)_2 \cdot 6\text{H}_2\text{O}$ ,  $\text{Cu}(\text{NO}_3)_2 \cdot 3\text{H}_2\text{O}$ ,  $\text{Mg}(\text{NO}_3)_2 \cdot 6\text{H}_2\text{O}$ , and  $\text{Zn}(\text{NO}_3)_2 \cdot 6\text{H}_2\text{O}$ ) was dissolved in 6 ml mixture of N, N-dimethylformamide (DMF, 99.8%) and ethanol (volume ratio of 3:1), followed by ultrasonication for 25 min to form the uniform metal precursor solution. Next, 1.56 mg organic linker (4,4'-bipyridine, BPY) and 10 mg surfactant (polyvinylpyrrolidone, PVP) were weighed and kept in a separate 20 ml glass vial. Subsequently, the metal precursor solution was added according to the desired molar ratio to the glass vial. Besides, 10 ml mixture of DMF and ethanol (volume ratio of 3:1) containing 4 mg 10,15,20-tetrakis(4-carboxyl-phenyl)-porphyrin (TCPP) solute was added dropwise into the aforementioned solution. The vial was then capped, sonicated for 25 min, and then heated to 80°C and kept at this temperature for 24 h to complete the solvothermal reaction. The red-colored product was washed with ethanol and separated via centrifugation at 8000 rpm for 10 min, and this step was repeated three times. Afterwards, the supernatant was removed and then the precipitates were dried at 60°C in the oven for 12 h to obtain the MOFs template.

Second, the MOFs template was annealed at different temperatures from 450 to 850°C for forming the single-phase HEO structure. When conducting at 850°C with a heating rate of 10°C min<sup>-1</sup> for 10 h in a flowing O<sub>2</sub> atmosphere, which is comparatively a lower temperature to form single phase HEO compared with published reports,<sup>18,30</sup> a black product with single phase denoted as HEO850 was obtained after quenching to room temperature. The complete process of HEO preparation is illustrated in Figure 1.

Furthermore, the annealing temperature on the product phase evolution was also evaluated at two different temperature values at 450 and 750, respectively. The samples so prepared are denoted as HEO450 and HEO750, respectively. For comparisons, MOFs with four (Ni, Co, Cu, and Zn) and two (Ni and Cu) metals were also prepared following similar procedures and were subsequently heated at 850°C to derive the medium entropy oxide (MEO) and low entropy oxide (LEO), respectively.

### 2.2 | Materials characterizations

The phase composition of the as-synthesized MOFs, HEO850, MEO, and LEO were analyzed by a Rigaku Smart Lab X-ray diffractometer (XRD) using a Cu K $\alpha$  radiation ( $\lambda = 0.154$  nm) at the scan range of 5°–80° with the speed of 5° min<sup>-1</sup>. Distinct morphologies of HEO850 were inspected under a scanning electron microscope (SEM, Tescan VEGA3) and a scanning transmission electron microscope (STEM, JEOL-2100F), both equipped with the energy-dispersive X-ray spectrometer (EDX). The chemical composition was investigated with an X-ray photoelectron spectrometer (XPS, Thermo Scientific Nexsa) and a Raman spectrometer (Renishaw Micro-Raman Spectroscopy System) with the 532 nm laser as the excitation source. The N<sub>2</sub> adsorption/desorption isotherms at 77 K were collected on a Micromeritics ASAP 2020 system, and the Brunauer–Emmett–Teller (BET) and Barrett–Joyner–Halenda (BJH) methods were applied to obtain the specific surface area and the pore size, respectively. The thermalgravimetric analyses were attained by a thermogravimetric analyzer/differential scanning calorimeter (TGA-DSC, Mettler Toledo TGA/DSC3+) in air with a ramp of 1°C min<sup>-1</sup>.

### 2.3 | Preparation of cathodes and electrochemical measurements

The HEO850/S/KB composite was prepared through the melt diffusion method by annealing the sulfur (S<sub>8</sub>, 70 wt.%), ketjen black (KB, EC-600JD, 20 wt.%), and HEO850 (10 wt.%) in an Ar-filled autoclave at 155°C for 12 h. As a result, the actual sulfur content in the composite is ~69%, determined by the TGA-DSC results (Figure S1). Similarly, the MEO/S/KB, LEO/S/KB, and S/KB composites were obtained as samples for comparison. The cathodes for Li-S batteries were fabricated from the homogeneous slurry containing 90 wt.% HEO850/S/KB (or MEO/S/KB, LEO/SKB, and S/KB) composite and 10 wt.% polyvinylidene fluoride (PVDF) binder in the N-methyl pyrrolidinone (NMP), which was uniformly coated onto the Al foil followed by cutting the electrode into 10 mm round disks. The areal sulfur loading in the prepared cathodes is generally 1 ~ 1.2 mg cm<sup>-2</sup>. Besides, the cathodes with a higher areal sulfur loading of ~4.4 mg cm<sup>-2</sup> were also obtained by casting the same slurry onto the carbon cloth. The CR-2025 coin cells were assembled in an Ar-filled glove box with Li metal as the anode, Celgard 2400 membrane as the separator, and 1 M bis (trifluoromethane) sulfonamide lithium salt (LiTFSI) dissolved in 1,3-dioxolane (DOL) and 1,2-dimethoxyethane (DME) (volume ratio of 1:1) with

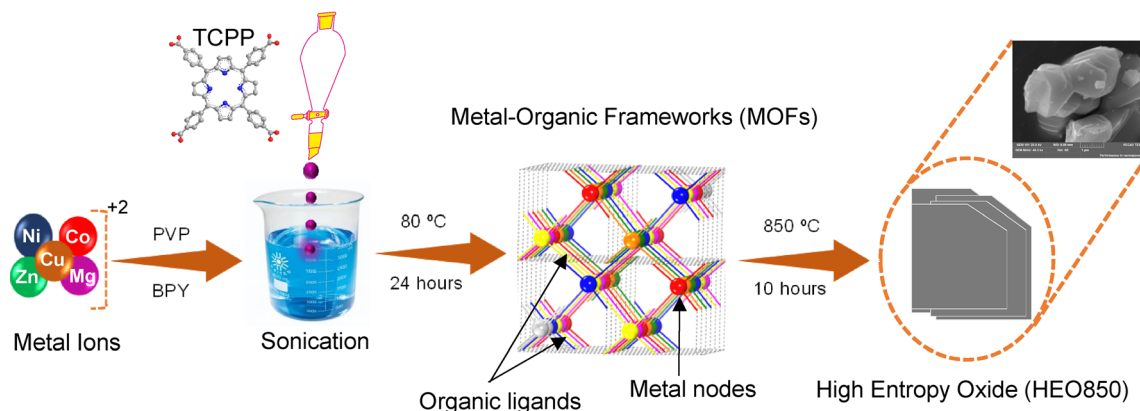


FIGURE 1 Schematic illustration of High entropy oxides (HEOs) preparation.

1 wt.%  $\text{LiNO}_3$  served as the electrolyte. The assembled coin cells were galvanostatically discharged and charged between 1.7 and 2.8 V (vs.  $\text{Li/Li}^+$ ) at different rates using a CT2001A cell test instrument (LAND Electronic Co.) at room temperature of 25°C. The specific capacities are calculated based on the mass loading of sulfur. Cyclic voltammetry (CV) at a scan rate of  $0.1 \text{ mV s}^{-1}$  from 1.7 to 2.8 V and electrochemical impedance spectroscopy (EIS) in the frequency range of 10 000 to 0.01 Hz were collected from a Metrohm Autolab electrochemical workstation under ambient conditions (25°C and 1 atm).

### 3 | RESULTS AND DISCUSSION

#### 3.1 | Phase evolution, reversibility, and configuration entropic dependency of HEO850

The XRD patterns depict the MOF structures<sup>31</sup> (Figure S2), and the TGA result signifies that a relatively low annealing temperature is enough to obtain the HEO from the self-sacrificing MOFs template (Figure S3). The initial annealing temperature was designed at 450°C, but the as-obtained sample contained multiphase without the well-known rock-salt one (Figure 2A).<sup>18</sup> By increasing the annealing temperature to 750°C, the relatively more intensified XRD peaks could be achieved because of the increased crystallinity, while the prominent peaks were well attributed to the rock-salt phase. However, several stray peaks still exist indicating the presence of the metal oxide impurities, including  $\text{Co}_3\text{O}_4$ ,  $\text{ZnO}$ , and  $\text{CuO}$ . Finally, at 850°C, the impurities are vanished leading to the single rock-salt phase with intensified sharp peaks at around 36.7°, 42.7°, 62.0°, 74.2°, and 78.1° corresponding to the (111), (222), (220), (310), and (222) rock-salt crystallographic planes, respectively.<sup>18</sup>

Furthermore, if entropy is the driving force to minimize the Gibbs free energy (Equation 1) towards the phase stabilization, the following conditions should be satisfied: (i) transition from multiphase to single phase should be reversible within a specific temperature range; (ii) systematic removal of compositional elements should destabilize the solid solution phase.<sup>18</sup>

$$\Delta G_{\text{mix}} = \Delta H_{\text{mix}} - T\Delta S_{\text{mix}} \quad (1)$$

To verify the former, the as-obtained HEO850 was further annealed at 750°C. Interestingly, many impure phases were observed, and the single rock-salt phase could be recovered again by thermally annealing at 850°C. It indicates that the phase is purely reversible within the temperature range of 750–850°C (Figure 2A).<sup>18</sup> Additionally, a slight shift of the XRD peaks towards lower angles upon annealing at a temperature higher than 750°C was also detected, implying the solid dissolution of the mixed metals oxides into a single rock-salt phase (Figure S4). For the latter, systematic elimination of the metal elements from the HEO850 composition was employed. The MEOs in Figure 2B denote the samples with one metal element removed from the HEO with details given in Table S1. The nonexistence of any single phase in MEOs at 850°C (Figure 2B) implies that the configurational entropic variation can significantly alter the transition temperature, and five or more metal cations are necessary to form the single-phase HEO. As the proof of concept, MOFs with two metal cations were also annealed at identical conditions, and the products were found not in a single-phase (Figure S5).

Furthermore, the deviation of the metal cations from the equimolar to the non-equimolar composition (Table S2) also led to the formation of impure phases (Figure S6). These results indicate that the obtained HEO850 at the relatively low temperature from the self-



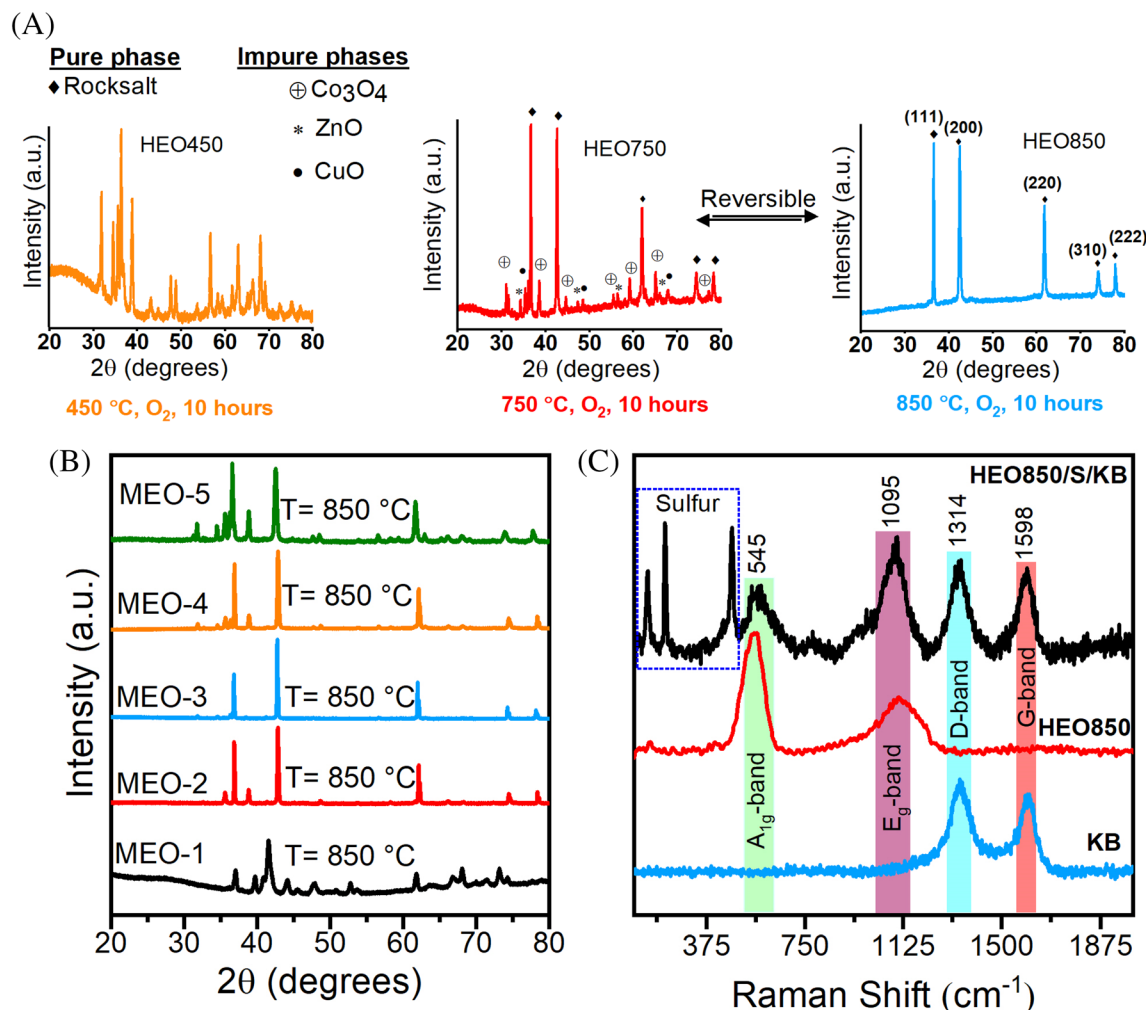


**FIGURE 2** (A) X-ray diffractometer (XRD) patterns depicting the phase evolution and reversibility; (B) Nonexistence of a single phase through configurational entropy variation; (C) Raman spectra of HEO850, KB, and HEO850/S/KB.

sacrificing MOFs template is the “high entropy-stabilized oxide”. The crystal structure of HEO850 was likewise identified by Raman spectroscopy in the range of 50–1400 cm<sup>-1</sup>. The strong band at 545 cm<sup>-1</sup> and the band at 1095 cm<sup>-1</sup> are ascribed to the A<sub>1g</sub> (LO) and E<sub>g</sub> (TO) of the rock-salt structure with the Fm-3m space group, respectively,<sup>32</sup> identical to the reported rock-salt structures like NiO LiMgYO<sub>3</sub> (Y=Sn, Ti, Zr).<sup>33–35</sup> After the HEO850/S/KB composite was prepared through S melt diffusion, these bands are still identifiable along with the D- and G-bands of KB (Figure 2C).

### 3.2 | Structure and morphology of HEO850

HEO850 exhibits the irregular morphologies with the particle size of ~300 nm (Figure 3A). The high-resolution transmission electron microscopy (HRTEM) image with clear lattice fringes depicts that it has high crystallinity

and a d-spacing of 0.21 nm corresponding to the (200) plane of the rock-salt structure (Figure 3B). The selected area electron diffraction (SAED) with ring patterns further confirms that HEO850 is polycrystalline (Figure 3C), in agreement with the XRD results (Figure 2A). Meanwhile, the STEM-EDX elemental mapping clearly shows the homogenous distribution of the constitutional Ni, Cu, Co, Mg, Zn, and O elements throughout the HEO850 particles without any specific element segregation (Figure 3D). Furthermore, the SEM and EDX spectrum suggest the approximately equimolar existence of five metal cations (Figure 3E,F). The specific surface area and the most available pore size are determined to be 10.7 m<sup>2</sup> g<sup>-1</sup> and 16.9 nm, respectively, which could contribute to the enhancement of the interaction between HEO850 and LiPSs (Figure S7). XRD patterns before and after S melt diffusion confirm the formation of HEO850/S/KB composite in the fabricated cathode of Li-S batteries (Figure 3G).

Furthermore, the chemical states of HEO850 were analyzed by XPS measurement. The survey spectrum reveals

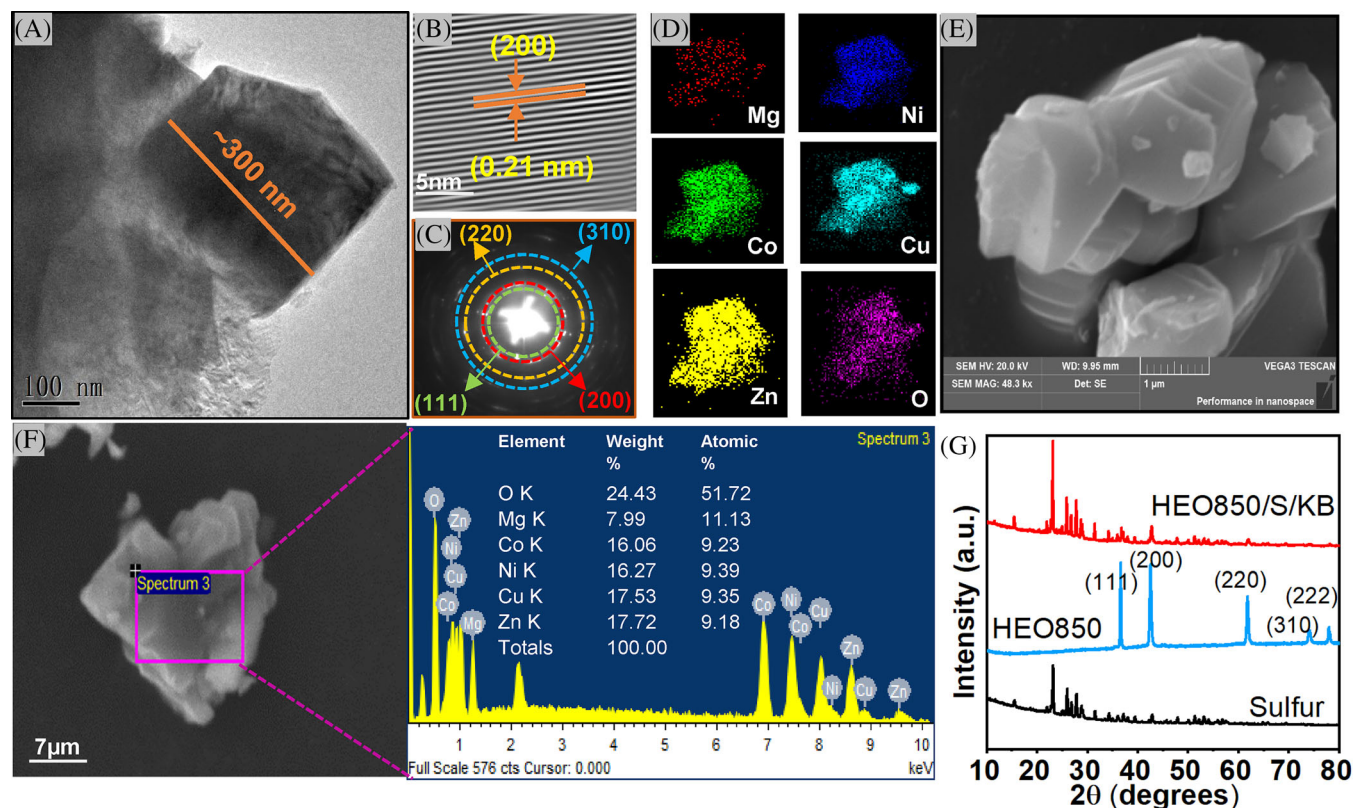


**FIGURE 3** (A) Transmission electron microscopy (TEM) image; (B) HETRM image; (C) SAED pattern; (D) STEM-EDX elemental mapping; (E) SEM micrographs; (F) SEM-EDX representing the equimolar metal elements; (G) X-ray diffractometer (XRD) patterns of HEO850/S/KB composite and solely HEO850 and sulfur.

the existence of the Ni, Co, Cu, Mg, Zn, and O elements (Figure S8), which matches well with the above-mentioned EDX results. The high-resolution XPS spectra (Figure S9) for HEO850 represent the distinct peaks of Zn 2p<sub>3/2</sub>, Zn 2p<sub>1/2</sub>, and Mg 1s with the respective binding energy of 1020.8, 1044.1, and 1302.5 eV, indicating the +2 valence state of both the Mg and Zn.<sup>36</sup> Besides, the satellite peaks in the core-level Cu 2p spectrum suggest that Cu is also in the +2 valence state.<sup>37</sup> Similarly, the binding energies at 796.1 eV for the 2p<sub>1/2</sub> core-level peak, 780.9 eV for the 2p<sub>3/2</sub> photoemission peak, and 785.9 and 803.5 eV for the respective 2p<sub>3/2</sub> and 2p<sub>1/2</sub> satellite peaks were detected in the Co 2p XPS spectrum, implying the +2 valence state for Co.<sup>38</sup> As for the Ni 2p XPS spectrum, the prominent peak confirms that Ni is also in the +2 valence state, but the intense shoulder satellite peaks with higher binding energies indicate the existence of +3 valence state for Ni.<sup>25,39</sup>

### 3.3 | Electrochemical testing

The electrochemical characteristics of the HEO850/S/KB and S/KB composite cathodes were evaluated by the cyclic voltammetry (CV) in the voltage range of 1.7–2.8 V

(vs. Li/Li<sup>+</sup>) at 0.1 mV s<sup>-1</sup> (Figure 4A). Two prominent cathodic reduction peaks in the voltage ranges of 2.2–2.28 V (peak I) and 1.9–2.02 V (peak II) are observed and could be associated with the reduction of sulfur (S<sub>8</sub>) into the soluble long-chain polysulfides Li<sub>2</sub>S<sub>x</sub> (4 ≤ x ≤ 8) and the subsequent conversion of these species to the insoluble Li<sub>2</sub>S<sub>2</sub>/Li<sub>2</sub>S, respectively,<sup>40</sup> while two anodic oxidation peaks at 2.3–2.32 V (peak III) and 2.37–2.4 (peak IV) are also detected, characterizing the corresponding reverse reactions. Both the reduction peaks (i.e., peak I and peak II) of the HEO850/S/KB cathode are intensified with larger CV area and smaller voltage gaps of ~40 and ~300 mV from the corresponding oxidation peaks, as compared to the routine S/KB cathode with the voltage gaps of ~50 and ~320 mV, thus indicating the fast redox kinetics. The positive voltage shift for the reduction peak II is also more prominent in the HEO850/S/KB cathode, which implies the vital progress given the slow kinetics of the second discharge plateaus.<sup>41–43</sup> Additionally, overlapping CV curves during the first five cycles signifies the superior reversibility of the HEO850/S/KB cathode (Figure 4B). This enhanced redox kinetics could be attributed to the catalytic activity of HEO850, which efficiently converts the polysulfides in the ongoing reduction cycles.<sup>44</sup>

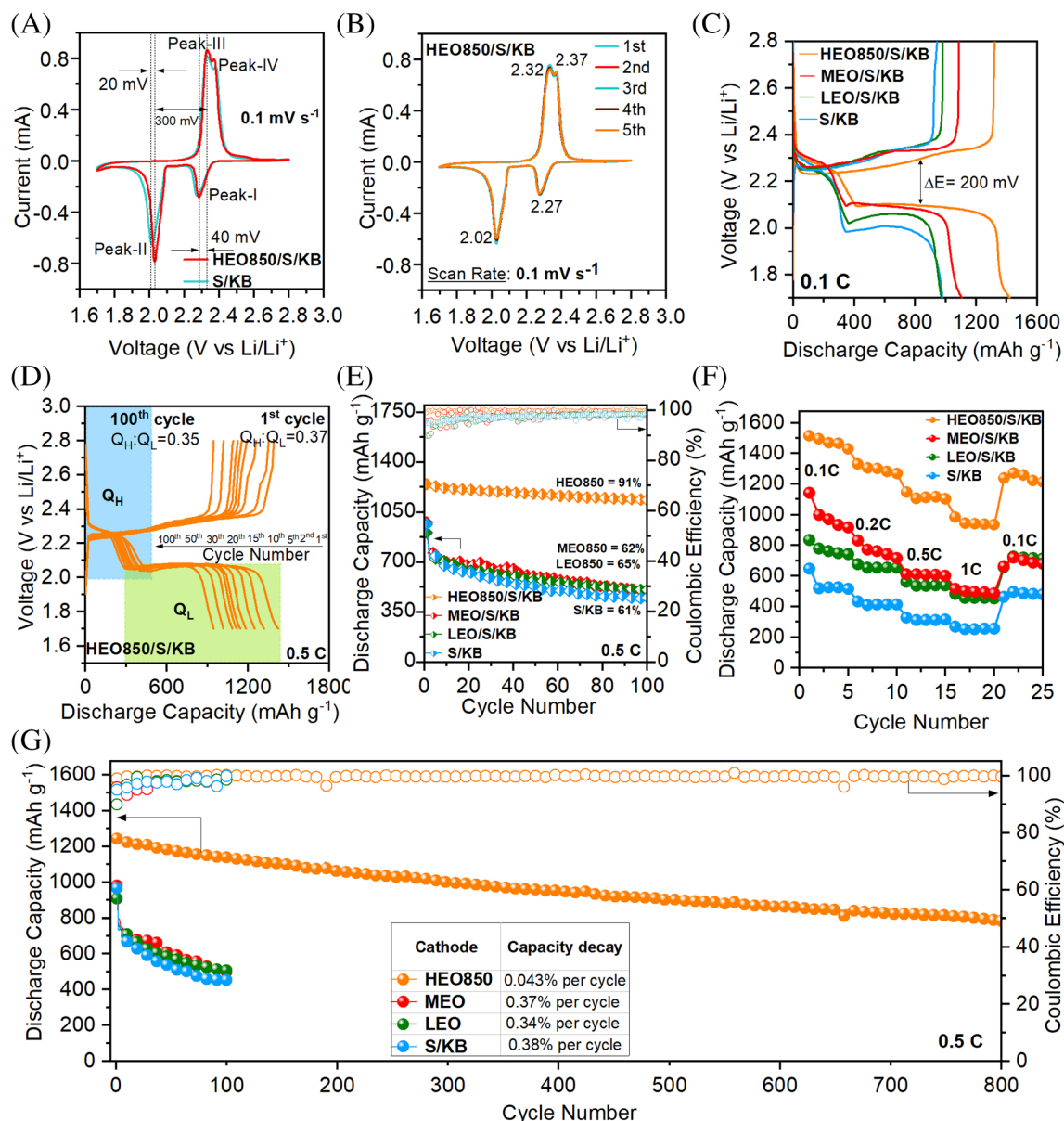


**FIGURE 4** (A) Comparison on cyclic voltammetry of HEO850/S/KB and S/KB cells; (B) CV curves of first five cycles of HEO850/S/KB cells at 0.1 mV s<sup>-1</sup>; (C) Galvanostatic charge and discharge plateaus at the 1st cycle of HEO850/S/KB, MEO850/S/KB, LEO850/S/KB and S/KB at 0.1 C; (D) Charge–discharge curves recorded for first 100 cycles at 0.5 C; (E) Cycling performance of HEO850/S/KB compared with MEO850/S/KB, LEO850/S/KB, and S/KB at 0.5 C for 100 cycles at E/S ratio of 15  $\mu\text{L mg}^{-1}$ ; (F) Comparison of rate performance at various C rate; (G) Comparison on long term cycling stability of HEO850/S/KB, MEO850/S/KB, LEO850/S/KB and S/KB cells at 0.5 C at E/S ratio of 15  $\mu\text{L mg}^{-1}$ .

Galvanostatic charge and discharge curves for the individual first cycle of the HEO850/S/KB, MEO850/S/KB, LEO850/S/KB and S/KB cells at 0.1 C are compared with results shown in Figure 4C, where the changes in the well-defined discharge plateaus reflect the electrochemical activity of the sulfur-containing cathodes. As the high voltage plateaus are accountable for the LiPSs diffusion and the well-known shuttling effect, efficient anchoring of these polysulfides within the cathodes can guarantee the higher discharge capacity in both the high-

voltage region and subsequent low-voltage regions. As expected, two discharge plateaus at  $\sim 2.3$  and  $\sim 2.03$  V and one charge plateaus at  $\sim 2.32$  V are prolonged for the HEO850/S/KB cathode as compared to the MEO850/S/KB, LEO850/S/KB and S/KB cathodes, which are consistent with the redox process as depicted in the CV curves and reveal the better electrochemical performance. Furthermore, the higher potential gap between the charge and discharge plateaus can imply the sluggish reaction from the soluble to the insoluble polysulfides and vice



versa. Thus, the evident lower polarization potential gap ( $\Delta E = \sim 200$  mV) of the HEO850/S/KB cathode in comparison with those of the MEO850/S/KB ( $\Delta E = \sim 240$  mV), LEO850/S/KB ( $\Delta E = \sim 260$  mV) and S/KB ( $\Delta E = \sim 280$  mV) cathodes could indicate the more efficient electrochemical redox reaction. The discharge capacity ( $Q_H$ ) from the high-voltage region is associated with the reduction of sulfur to the soluble long-chain polysulfides, while the capacity ( $Q_L$ ) from the low-voltage plateaus is due to the ongoing conversion of these polysulfides to the insoluble species. Figure 4D shows the charge/discharge curves of the HEO850/S/KB cathode at 0.5 C for the 1st, 2nd, 5th, 10th, 15th, 20th, 30th, 50th, and 100th cycles with a slight variation of  $Q_H/Q_L$  ratio from 0.37 to 0.35. This variation could be attributed to small increase in polarization with prolonged cycling. These results also indicate the facile and reversible conversion of both long and short chain polysulfides enabled by cumulative effect of the numerous randomly dispersed active sites in the HEO850. It is especially important as the higher concentration of soluble lithium polysulfides can significantly exacerbate the failure of the Li-S batteries.

Additionally, the cycling performance of the HEO850/S/KB, MEO850/S/KB, LEO850/S/KB, and S/KB cathodes at 0.5 C with the areal sulfur loading of  $\sim 1.2$  mg cm $^{-2}$  and the electrolyte to the sulfur ratio (E/S) of 15  $\mu$ l mg $_{\text{sulfur}}^{-1}$  is shown in Figure 4E. The HEO850/S/KB cathode delivered an initial discharge capacity of  $\sim 1244$  mAh g $^{-1}$ , which was retained at  $\sim 1137$  mAh g $^{-1}$  after 100 cycles with the superior retention of 91% and an average Coulombic efficiency of  $\sim 99.5\%$ . In contrast, MEO850/S/KB, LEO850/S/KB, and S/KB delivered lower initial discharge capacities of  $\sim 980$ ,  $\sim 908$ , and  $\sim 966$  mAh g $^{-1}$  with the capacity retention of 62%, 65%, and 61%, respectively. The outstanding cycling performance of the HEO850/S/KB cathode can be attributed to the more exposed active metal sites within high-entropy metal oxides to anchor LiPSs efficiently.

Rate performance of the HEO850/S/KB cathode is also compared with the MEO850/S/KB, LEO850/S/KB, and S/KB cathodes at the successive current densities of 0.1, 0.2, 0.5, 1, and 0.1C. As shown in Figure 4F, the HEO850/S/KB cathode displays the specific discharge capacities of  $\sim 1513$ ,  $\sim 1330$ ,  $\sim 1147$ ,  $\sim 985$ , and  $\sim 1236$  mAh g $^{-1}$  at different current densities with the 82% of capacity recovery on quick return to 0.1°C. In comparison, the MEO850/S/KB, LEO850/S/KB, and the routine S/KB cathodes only display the comparatively lower capacity along with inferior retention of 59%, 78%, and 72%, respectively. This superior electrochemical performance of the HEO850/S/KB cathode could be again attributed to the affluent and randomly dispersed active metal sites of HEO850 that capture the polysulfides efficiently. Moreover, the long-term cycling stability

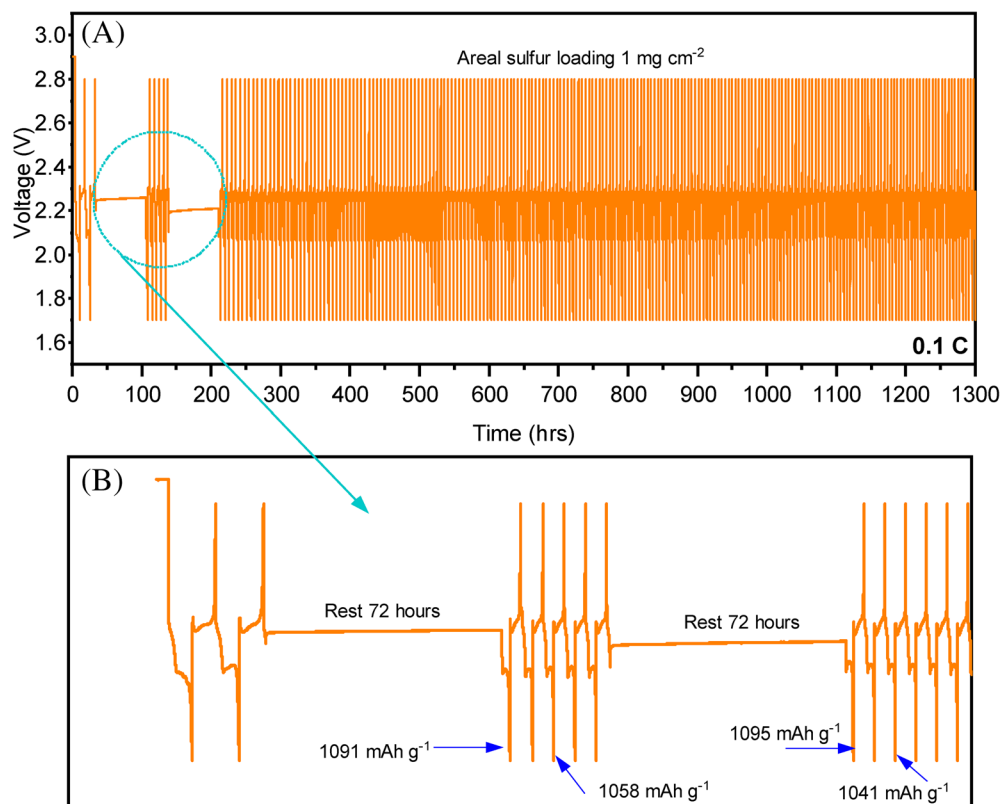
by virtue of LIPSS confinement is considered to be a decisive parameter that makes lithium-sulfur cells viable for practical applications. The first cycle-specific discharge capacity of HEO850/S/KB ( $\sim 1244$  mAh g $^{-1}$ ) is significantly higher than those of MEO850/S/KB (980 mAh g $^{-1}$ ), LEO850/S/KB (908 mAh g $^{-1}$ ), and S/KB (966 mAh g $^{-1}$ ), and the retention capacity is  $\sim 784$  mAh g $^{-1}$  with superior Coulombic efficiency of  $\sim 99.6\%$ , demonstrating outstanding cycling stability with a negligible capacity decay of 0.043% per cycle at 0.5 C after 800 cycles. Compared to HEO850/S/KB cells, MEO850/S/KB, LEO850/S/KB, and S/KB cells exhibited severe capacity decay and reached around  $\sim 500$  mAh g $^{-1}$  with a higher decay rate of 0.37%, 0.34%, and 0.38% after 100 cycles, as shown in Figure 4G. The electrochemical performances of HEO850/S/KB cathode in comparison to several literature reports are also summarized in Table S3.

Self-discharge is also one of the significant factors affecting the practical application of secondary Li-S battery. To identify the role of HEO850 as an inhibitor towards self-discharge, cells (with an areal sulfur loading of 1 mg cm $^{-2}$ ) were galvanostatically charged-discharged at 0.1 C and rested for 72 h at 2.2 and 2.1 V, respectively (Figure 5). The first cycle is considered as a conditioning cycle that makes the battery condition comparable, while the next cycle is for checking the regular capacity. In the 3rd cycle, the battery was discharged up to a specific voltage of 2.2 V and rested for 72 h, as shown in Figure 5A. During the resting period, the open-circuit voltage was monitored and found to have no significant drop while the cell capacity maintained within  $\sim 1091$  mAh g $^{-1}$  and  $\sim 1200$  mAh g $^{-1}$  (Figure 5B). Afterwards, the cell was charged and discharged for several cycles to check the regular capacity. Then, the 8th cycle was discharged to 2.1 V and rested for 72 h. Interestingly, after the resting processes, the cell delivered a capacity of  $\sim 1095$  mAh g $^{-1}$ , comparable to the regular discharged capacity of  $\sim 1058$  mAh g $^{-1}$  (Figure 5B). These results are consistent with those published in literature,<sup>45</sup> suggesting that there is no self-discharging in HEO850/S/KB in the second plateau. Hence, HEO850 could inhibit the polysulfide shuttling and facilitate the fast conversion of higher-order polysulfide to lower-order ones.

Moreover, with the rate increased to 2 C and 4 C, the HEO850/S/KB cathode can still present the stable cycling performance with the retention of 84% from the initial capacity of 699 mAh g $^{-1}$  at 2 C and that of 73% from 529 mAh g $^{-1}$  at 4 C (Figure 6A). Meanwhile, to verify the synergistic effect of the randomly distributed multi-metal in HEO850 in anchoring LiPSs, the performance of HEO850/S/KB cathode is compared with that of the single-metal oxide systems. The NiO/S/KB cathode was therefore assembled and controlled similarly, which exhibited poorer electrochemical performance with an



**FIGURE 5** Self-discharging of HEO850/S/KB at  $1 \text{ mg cm}^{-2}$ .



initial discharge capacity of  $\sim 737 \text{ mAh g}^{-1}$  at  $0.5 \text{ C}$  and 61% retention after 100 cycles (Figure 6B). It is evident that the affluent and randomly dispersed active metal sites exposed by HEO850 play a vital role in controlling LiPSs to ensure the stable cycling performance of Li-S batteries. When the sulfur loading is increased from  $\sim 1.2$  to  $\sim 4.4 \text{ mg cm}^{-2}$ , in first few cycles the HEO850/S/KB cathode and S/KB cathode exhibits comparable electrochemical performance. Afterwards the positive catalytic effect of HEO850 could be seen, which accelerated reaction kinetics, and the battery showed stable cycling for 100 cycles with capacity retention of 85% with respect to initial discharge capacity of  $1044 \text{ mAh g}^{-1}$  at  $0.1 \text{ C}$ . In comparison, bare S/KB electrodes displayed poorer performance and its capacity retention dropped to 63% after 80 cycles because of sluggish reaction and possible shuttle effect without HEO850 (Figure 6C). As low E/S ratio is crucial for the practical application of Li-S batteries. Figure S10 shows the stable cycling performance of HEO850/S/KB cathode at low E/S ratio of  $5 \mu\text{l mg}^{-1}$ . The HEO850/S/KB cathode at high sulfur loading of  $4.4 \text{ mg cm}^{-2}$  delivered initial discharge capacity of  $\sim 850 \text{ mAh g}^{-1}$  at  $0.1 \text{ C}$  and retained at  $\sim 690 \text{ mAh g}^{-1}$  after 50 discharge-charge cycles. These results indicate the feasibility of fabricated HEO850 with novel MOFs template method for Li-S batteries. Furthermore, the bulk electrolyte resistance of the HEO850/S/KB, MEO/S/KB, LEO/S/KB, and S/KB cathodes obtained from the EIS

measurement is comparable at the high-frequency region. In contrast, the semicircle at the middle-frequency region of HEO850/S/KB is significantly smaller, indicating a favorable lessening of the interfacial impedance between the electrode and electrolyte to enhance the charge transfer effectively (Figure 6D). The relatively small impedance also suggests the Li-ion transporting behavior in the HEO850/S/KB cathode could be improved, which ultimately benefits the enhanced electrochemical activity of the sulfur electrodes for Li-S batteries.

To probe the catalytic performance of HEO850 during the polysulfide conversion processes, symmetric cells with HEO850/KB acting as both the working and counter electrodes and cells with KB were assembled using  $0.2 \text{ M Li}_2\text{S}_6$  as the electrolyte. The CV tests were first carried out at a scan rate of  $10 \text{ mV s}^{-1}$  in the voltage window of  $-1$  to  $1 \text{ V}$ . As displayed in Figure 7A, the HEO850/KB cell exhibits distinct and more significant current density than the KB cell, demonstrating that HEO850 is beneficial for the fast conversion of LiPSs.<sup>46</sup> To further investigate the reaction kinetics, the CV measurements of the HEO850/S/KB and S/KB cells at various scan rates from  $0.1$  to  $0.5 \text{ mV s}^{-1}$  were conducted (Figure 7B,C). Although the increase in the scan rate does not bring in any significant variation of the shape of CV curves, indicating electrochemical stability, the slope of the linear fitting of the maximum peak current and the square root of the scan rate ( $I_p/V^{0.5}$ ) is higher for the HEO850/S/KB

cathode than the bare S/KB cathode, thus validating the fast ion diffusion (Figure 7D–F).

### 3.4 | Anchoring mechanism investigation

To further evaluate the catalytic activity of HEO850 and its interaction with LiPSs, ex-situ XPS analyses on the HEO850/S/KB cathode before and after 100 cycles were carried out, where the interaction was mainly manifested by the Mg 1s, Ni 2p, Zn 2p, and O1s spectra. The XPS peak for Mg 1s at 1302.5 eV is integrally shifted to 1304.9 eV with an obvious shift of 2.4 eV after cycling (Figure 8A), while the peaks for Ni 2p<sub>3/2</sub> and Ni 2p<sub>1/2</sub> are respectively shifted by 3.1 and 4.3 eV towards higher binding energies (Figure 8B). The results indicate that Mg and Ni may contribute to the vigorous redox activity and prominent interaction between HEO850 and LiPSs. The binding energies of Zn 2p<sub>3/2</sub> displayed a positive shift of 1.3 eV (Figure 8C), indicating the interaction of LiPSs and HEOs and these results are also in accordance with the published report.<sup>30</sup> Furthermore, the high-resolution

spectra of O 1s showed a positive shift of 0.6 eV after cycling (Figure 8D), which resulted from the interaction of Li and O presumably.<sup>17,47,48</sup> According to previous studies, raising the binding energy of O1s would increase the activity and mobility of oxygen species, which could facilitate the bonding of O species in HEO to Li species in LiPSs.<sup>49</sup> These XPS results revealed that large peak shift (0.6 ~ 2.0 eV) of metal elements should be attributed to the chemical reactions of HEO850 with polysulfides during cycling processes which was further confirmed in ex-situ XRD.

The morphology evolution of the HEO850/S/KB cathode before and after cycling at 0.5 C is also observed. The porous structure significantly disappears after cycling (Figure S11), which could be due to the contact between the cathodes and the electrolyte and is beneficial to the decrease in the transport distances of LiPSs and electrons. This could further contribute to the enhanced electrochemical performance.

As an important analysis means, the ex-situ XRD measurement is performed with 2 $\theta$  ranging from 28° to 64°, which could probe the structural stability of HEO850 during the electrochemical processes. The HEO850/S/KB

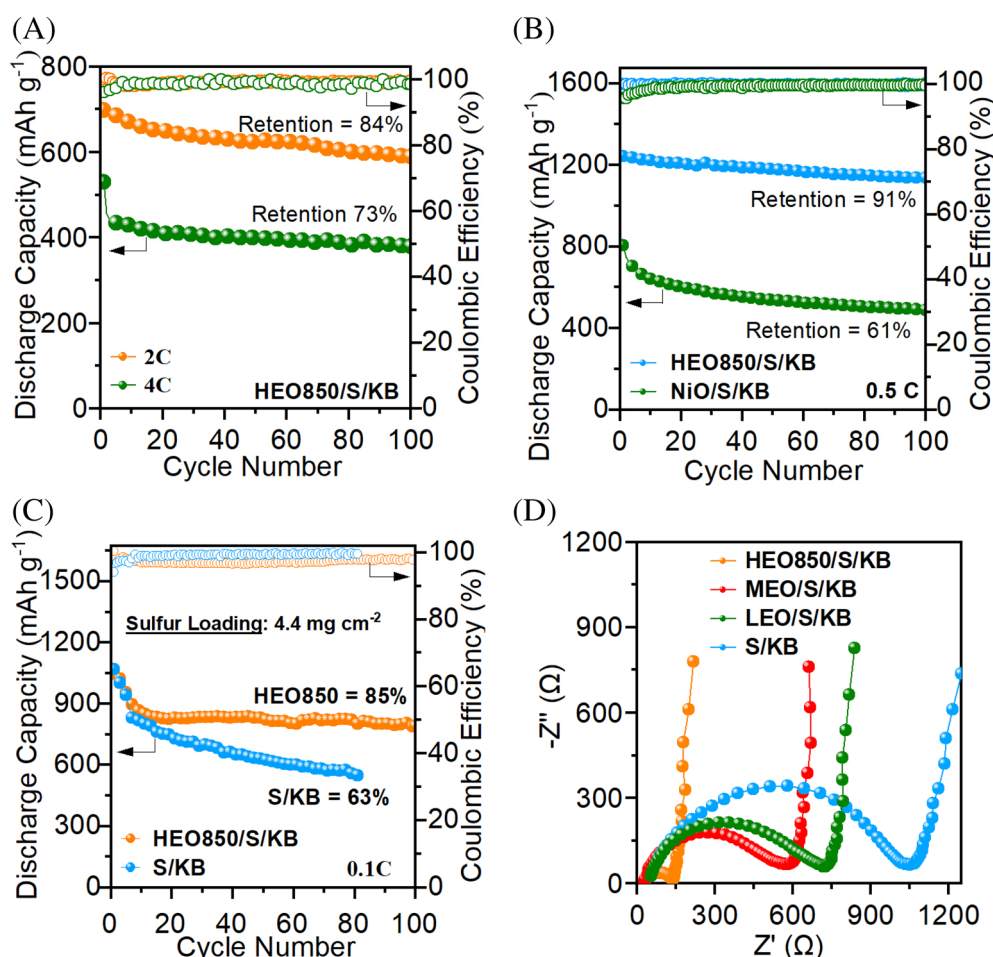
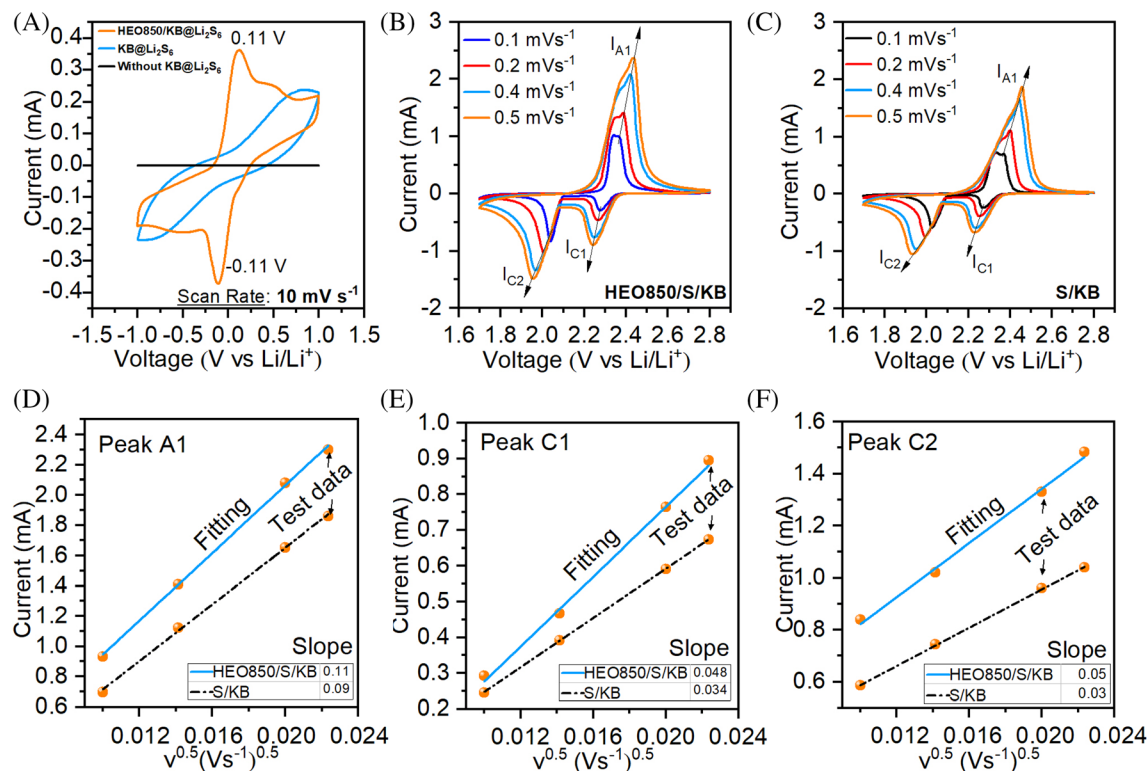


FIGURE 6

(A) Electrochemical performance at the rates of 2 C and 4 C at E/S ratio of 15  $\mu\text{L mg}^{-1}$ ; (B) Comparison on the electrochemical performance of HEO850 with NiO at E/S ratio of 15  $\mu\text{L mg}^{-1}$ ; (C) Cycling performance at 0.1 C with higher sulfur loading (4.4  $\text{mg cm}^{-2}$ ) at E/S ratio of 15  $\mu\text{L mg}^{-1}$ ; (D) Electrochemical impedance spectra of HEO850/S/KB, MEO850/S/KB, LEO850/S/KB, and S/KB cathodes.



**FIGURE 7** (A) CV curves of symmetric cells demonstrating the catalytic activity of HEO850; (B) CV curves of HEO850/S/KB cells at various scan rates; (C) CV curves of S/KB cathode at various scan rates; (D) Linear fitting for the anodic peak (A1) current and the square root of scan rate; (E) Linear fitting for the cathodic peak (C1) current and the square root of scan rate; (F) Linear fitting for the cathodic peak (C2) current and the square root of scan rate.

cells were discharged and charged up to specific cut-off voltages, which were then disassembled for the XRD measurement (Figure 9). The XRD peak at 33.5° is associated with Li<sub>2</sub>O in the disassembled cathode after discharging down to a voltage of 2.0, 1.9, 1.8, or 1.7 V. It also appears upon charging at 2.1 V because there are more Li<sup>+</sup> presenting in the cathode (HEO850/S/KB) when exposed in air. This peak disappears for the cathode upon charging at 2.3 to 2.8 V because the Li<sup>+</sup> move towards the lithium metal anode. Interestingly, during the discharge process (2.0 to 1.7 V), two obvious peaks at ~29.7° and ~34.7° emerge and could be ascribed to MgS (PDF#04-007-3406) and NiS (PDF#00-002-1280), respectively. Both peaks are disappeared on subsequent charging process (2.3 to 2.7 V), indicating that Mg and Ni play the vital role in efficient polysulfide anchoring via chemically reacting with polysulfides, which is ultimately favorable for the long cycling life of the battery. These are also consistent with the XPS results (Figure 8) that indicate the chemical reaction of HEO850 with lithium polysulfides during the redox cycling process. In parallel, the peak at ~34° of the fully charged cell (2.7 V) suggests that the higher lithium polysulfides are converted to the elemental sulfur (S<sub>8</sub>). Nevertheless, the strong peaks at

36.7°, 42.7°, and 62.0° for HEO850 remained unchanged during discharging and charging processes, confirming that the HEO850 structure is stable. In addition, we have also observed that HEO850 had transitioned from oxide to sulfide, including NiS<sub>2</sub>, Cu<sub>7</sub>S<sub>4</sub>, and CoS phases which may also play the catalytic role for stable cycling.

These results indicate that, the LiPSs could be effectively anchored by the exposed active sites of HEO850 during charging and discharging cycles, according to XPS and ex-situ XRD data. Ni, Zn, Mg, and O, in particular, were critical in chemically encapsulating the shuttle species. The chemical anchoring effect causes considerable shifts in the peaks in XPS spectra of the aforementioned metal species of HEO850, implying mutual electron transfer between HEO850 and LiPSs, which is advantageous for enhanced electrochemical performance. In summary, the XPS analysis examines the interaction between HEO850 and LiPSs and finds that the bonding effect of Li-O and Ni-S significantly improves polysulfide immobilization and that the synergistic effect of multielement in HE850 contributes to polysulfide absorption and electrochemical conversion. Meanwhile, ex-situ XRD confirmed that anchoring phenomenon continues during the charge and discharge process without imparting structural changes on HEO850.



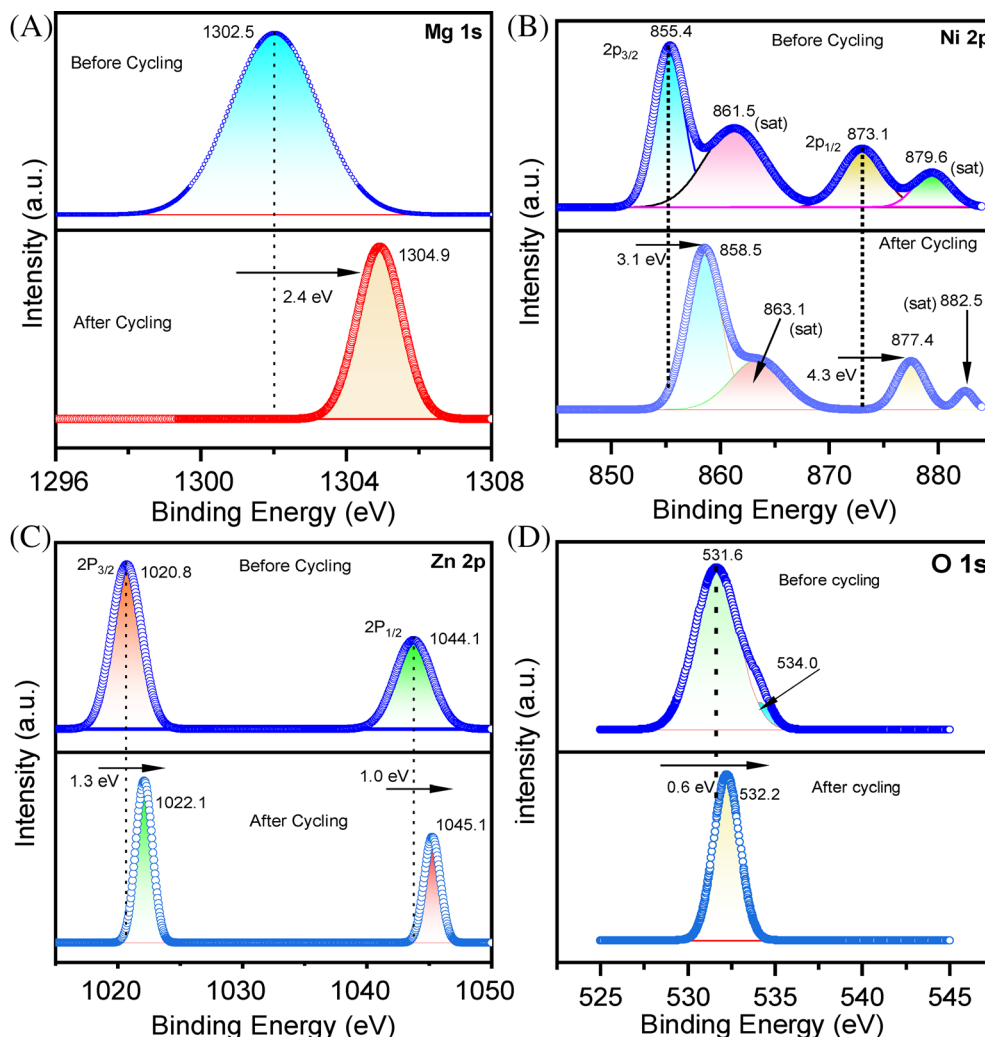


**FIGURE 8** High-resolution X-ray photoelectron spectrometer (XPS) spectra of (A) Mg 1s, (B) Ni 2p, (C) Zn 2p, and (D) O 1s before and after 100 cycles at 0.5 C.

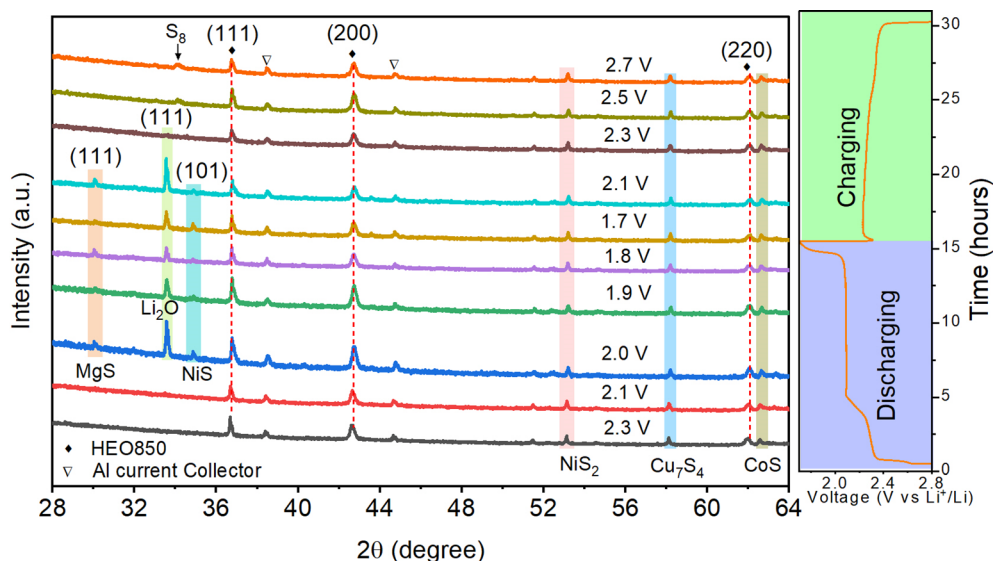


**FIGURE 9** Ex-situ X-ray diffractometer (XRD) measurement on the HEO850/S/KB cathode at various discharging and charging conditions.

## 4 | CONCLUSION

In conclusion, an effective sulfur-host material, that is, HEO850, is successfully synthesized through a novel low-

temperature template route by employing the self-sacrificing *M*-MOFs. The as-obtained HEO containing five homogeneously distributed metal elements, that is, Ni, Mg, Cu, Zn, and Co, exhibits a single-phase rock-salt

structure. By tuning the synthesis temperature and the composition of HEO, the obtained HEO850 is proved to exhibit entropy-dominated phase stabilization. When used in the Li-S batteries, the HEO850/S/KB cathode exhibits improved specific discharge capacity of  $\sim 1513$ ,  $\sim 1330$ ,  $\sim 1147$ , and  $\sim 985$  mAh g $^{-1}$  at 0.1 C, 0.2 C, 0.5 C, 1 C, respectively, which could be retained at  $\sim 1236$  mAh g $^{-1}$  after returning to 0.1 C. The HEO850/S/KB performs much superiorly to those of MEO850/S/KB, LEO850/S/KB, and S/KB cathodes. As for the cycling stability, the HEO850/S/KB cathode can deliver a specific initial discharge capacity of 1244 mAh g $^{-1}$  at 0.5 C, in comparison with those of MEO850/S/KB ( $\sim 980$  mAh g $^{-1}$ ), LEO850/S/KB ( $\sim 908$  mAh g $^{-1}$ ), and S/KB ( $\sim 966$  mAh g $^{-1}$ ). The HEO850/S/KB could retain its capacity at 784 mAh g $^{-1}$  with an enhanced Coulombic efficiency of  $\sim 99.6\%$  after 800 cycles and a capacity decay of 0.043% per cycle. This excellent electrochemical performance could be attributed to the catalytic activity of HEO850 that can efficiently anchor LiPSs. This work demonstrates that HEO enhances the electrochemical performance of Li-S batteries through efficient chemical immobilization of LiPSs and provides a novel technique to synthesize the entropy-stabilized HEOs at a relatively low annealing temperature (850°C) for energy conversion and storage applications.

## AUTHOR CONTRIBUTIONS

**Hassan Raza:** Conceptualization, Data curation, Formal analysis, Initial draft writing; **Junye Cheng:** Supervision, Formal analysis, Conceptualization, Review Editing; **Cong Lin and Soumyadip Majumder:** Formal analysis, Conceptualization, Review Editing; **Guohua Chen:** Supervision, Funding acquisition, Conceptualization, Review-Editing.

## ACKNOWLEDGMENTS

Hassan Raza acknowledges the international postgraduate scholarship (IPS) support from the Hong Kong Polytechnic University, China. All authors are grateful for the financial support from the R&D Projects in Key Areas of Guangdong Province (Grant No. 2019B090908001), Science, Technology, and Innovation Commission of Shenzhen Municipality (Grant No. SGDX20190816230615451), the Guangdong Province Science & Technology Bureau (Grant No. 2020A0505090011), and Guangdong-Hong Kong-Macao Joint Lab for Photonic-Thermal-Electrical Energy Materials and Devices (Grant No. 2019B121205001).

## CONFLICT OF INTEREST

The authors declare no conflict of interest.

## DATA AVAILABILITY STATEMENT

The raw data required to reproduce these findings are available from the corresponding author upon reasonable request.

## ORCID

Hassan Raza  <https://orcid.org/0000-0002-0613-0186>

Junye Cheng  <https://orcid.org/0000-0001-5504-8528>

Cong Lin  <https://orcid.org/0000-0003-0021-5055>

## REFERENCES

- Manthiram A, Fu Y, Chung SH, Zu C, Su YS. Rechargeable lithium-sulfur batteries. *Chem Rev*. 2014;114(23):11751-11787. doi:10.1021/cr500062v
- Song J, Xu T, Gordin ML, et al. Nitrogen-doped mesoporous carbon promoted chemical adsorption of sulfur and fabrication of high-areal-capacity sulfur cathode with exceptional cycling stability for lithium-sulfur batteries. *Adv Funct Mater*. 2014;24(9):1243-1250. doi:10.1002/adfm.201302631
- Larcher D, Tarascon JM. Towards greener and more sustainable batteries for electrical energy storage. *Nat Chem*. 2015;7(1):19-29. doi:10.1038/nchem.2085
- Liu X, Huang J-Q, Zhang Q, Mai L. Nanostructured metal oxides and sulfides for lithium-sulfur batteries. *Adv Mater*. 2017;29(20):1601759. doi:10.1002/adma.201601759
- Jing H-K, Kong L-L, Liu S, Li G-R, Gao X-P. Protected lithium anode with porous Al<sub>2</sub>O<sub>3</sub> layer for lithium-sulfur battery. *J Mater Chem A*. 2015;3(23):12213-12219. doi:10.1039/C5TA01490E
- Fang R, Zhao S, Sun Z, Wang DW, Cheng HM, Li F. More reliable lithium-sulfur batteries: status, solutions and prospects. *Adv Mater*. 2017;29(48):1606823. doi:10.1002/adma.201606823
- Su Y-S, Manthiram A. Lithium-sulphur batteries with a micro-porous carbon paper as a bifunctional interlayer. *Nat Commun*. 2012;3(1):1-6.
- Guo J, Xu Y, Wang C. Sulfur-impregnated disordered carbon nanotubes cathode for lithium-sulfur batteries. *Nano Lett*. 2011;11(10):4288-4294. doi:10.1021/nl202297p
- Ji X, Lee KT, Nazar LF. A highly ordered nanostructured carbon-sulphur cathode for lithium-sulphur batteries. *Nat Mater*. 2009;8(6):500-506. doi:10.1038/nmat2460
- Carter R, Ejorh D, Share K, et al. Surface oxidized mesoporous carbons derived from porous silicon as dual polysulfide confinement and anchoring cathodes in lithium sulfur batteries. *J Power Sources*. 2016;330:70-77. doi:10.1016/j.jpowsour.2016.08.128
- Xin S, You Y, Li H-Q, et al. Graphene sandwiched by sulfur-confined mesoporous carbon nanosheets: A kinetically stable cathode for Li-S batteries. *ACS Appl Mater Interfaces*. 2016;8(49):33704-33711. doi:10.1021/acsami.6b12142
- Borchardt L, Oschatz M, Kaskel S. Carbon materials for lithium sulfur batteries—ten critical questions. *Chem-A Eur J*. 2016;22(22):7324-7351. doi:10.1002/chem.201600040
- Liang X, Hart C, Pang Q, Garsuch A, Weiss T, Nazar LF. A highly efficient polysulfide mediator for lithium-sulfur batteries. *Nat Commun*. 2015;6(1):1-8.
- Carter R, Oakes L, Muralidharan N, Cohn AP, Douglas A, Pint CL. Polysulfide anchoring mechanism revealed by atomic layer deposition of V<sub>2</sub>O<sub>5</sub> and sulfur-filled carbon nanotubes for lithium-sulfur batteries. *ACS Appl Mater Interfaces*. 2017;9(8):7185-7192. doi:10.1021/acsami.6b16155
- Sun Q, Xi B, Li JY, et al. Nitrogen-doped graphene-supported mixed transition-metal oxide porous particles to confine

- polysulfides for lithium-sulfur batteries. *Adv Energy Mater.* 2018;8(22):1800595. doi:10.1002/aenm.201800595
16. Zhang Y, Zhao Y, Yermukhambetova A, Bakenov Z, Chen P. Ternary sulfur/polyacrylonitrile/Mg<sub>0.6</sub>Ni<sub>0.4</sub>O composite cathodes for high performance lithium/sulfur batteries. *J Mater Chem A.* 2013;1(2):295-301. doi:10.1039/C2TA00105E
  17. Kong L, Chen X, Li BQ, et al. A bifunctional perovskite promoter for polysulfide regulation toward stable lithium-sulfur batteries. *Adv Mater.* 2018;30(2):1705219. doi:10.1002/adma.201705219
  18. Rost CM, Sachet E, Borman T, et al. Entropy-stabilized oxides. *Nat Commun.* 2015;6(1):1-8.
  19. Nguyen T, Boudard M, Rapenne L, Carmezim MJ, Montemor MF. Morphological changes and electrochemical response of mixed nickel manganese oxides as charge storage electrodes. *J Mater Chem A.* 2015;3(20):10875-10882. doi:10.1039/C5TA01453K
  20. Mullens C, Pikulski M, Agachan S, Gorski W. Synergistic effects in multicomponent electrocatalysts: the Pb-Ir-O system. *J Am Chem Soc.* 2003;125(44):13602-13608. doi:10.1021/ja0366843
  21. Jiang S, Hu T, Gild J, et al. A new class of high-entropy perovskite oxides. *Scr Mater.* 2018;142:116-120. doi:10.1016/j.scriptamat.2017.08.040
  22. Sarkar A, Djenadic R, Wang D, et al. Rare earth and transition metal based entropy stabilised perovskite type oxides. *J Eur Ceram Soc.* 2018;38(5):2318-2327. doi:10.1016/j.jeurceramsoc.2017.12.058
  23. Biesuz M, Spiridigliozzi L, Dell'Agli G, Bortolotti M, Sglavo VM. Synthesis and sintering of (Mg, Co, Ni, Cu, Zn)O entropy-stabilized oxides obtained by wet chemical methods. *J Mater Sci.* 2018;53(11):8074-8085. doi:10.1007/s10853-018-2168-9
  24. Wang Q, Sarkar A, Wang D, et al. Multi-anionic and -cationic compounds: new high entropy materials for advanced Li-ion batteries. *Energ Environ Sci.* 2019;12(8):2433-2442. doi:10.1039/C9EE00368A
  25. Chen Y, Fong DD, Herbert FW, et al. Modified oxygen defect chemistry at transition metal oxide heterostructures probed by hard X-ray photoelectron spectroscopy and X-ray diffraction. *Chem Mater.* 2018;30(10):3359-3371. doi:10.1021/acs.chemmater.8b00808
  26. Sarkar A, Djenadic R, Usharani NJ, et al. Nanocrystalline multicomponent entropy stabilised transition metal oxides. *J Eur Ceram Soc.* 2017;37(2):747-754.
  27. Bérardan D, Franger S, Meena A, Dragoe N. Room temperature lithium superionic conductivity in high entropy oxides. *J Mater Chem A.* 2016;4(24):9536-9541. doi:10.1039/C6TA03249D
  28. Dąbrowa J, Stygar M, Mikula A, et al. Synthesis and microstructure of the (Co, Cr, Fe, Mn, Ni)<sub>3</sub>O<sub>4</sub> high entropy oxide characterized by spinel structure. *Mater Lett.* 2018;216:32-36. doi:10.1016/j.matlet.2017.12.148
  29. Yaghi O, Li H. Hydrothermal synthesis of a metal-organic framework containing large rectangular channels. *J Am Chem Soc.* 1995;117(41):10401-10402. doi:10.1021/ja00146a033
  30. Zheng Y, Yi Y, Fan M, et al. A high-entropy metal oxide as chemical anchor of polysulfide for lithium-sulfur batteries. *Energy Storage Mater.* 2019;23:678-683. doi:10.1016/j.ensm.2019.02.030
  31. Zhou G, Zhao Y, Manthiram A. Dual-confined flexible sulfur cathodes encapsulated in nitrogen-doped double-shelled hollow carbon spheres and wrapped with graphene for Li-S batteries. *Adv Energy Mater.* 2015;5(9):1402263. doi:10.1002/aenm.201402263
  32. Dąbrowa J, Stygar M, Mikula A, et al. Synthesis and microstructure of the (Co, Cr, Fe, Mn, Ni)<sub>3</sub>O<sub>4</sub> high entropy oxide characterized by spinel structure. *Mater Lett.* 2018;216:32-36. doi:10.1016/j.matlet.2017.12.148
  33. Wu H, Kim ES. Correlations between crystal structure and dielectric properties of high-Q materials in rock-salt structure Li<sub>2</sub>O-MgO-BO<sub>2</sub> (B = Ti, Sn, Zr) systems at microwave frequency. *RSC Adv.* 2016;6(53):47443-47453. doi:10.1039/C6RA06624K
  34. George G, Anandhan S. Synthesis and characterisation of nickel oxide nanofibre webs with alcohol sensing characteristics. *RSC Adv.* 2014;4(107):62009-62020. doi:10.1039/C4RA11083H
  35. Luo C, Li D, Wu W, Zhang Y, Pan C. Preparation of porous micro-nano-structure NiO/ZnO heterojunction and its photocatalytic property. *RSC Adv.* 2014;4(6):3090-3095. doi:10.1039/C3RA44670K
  36. Kheradmandfard M, Minouei H, Tsvetkov N, et al. Ultrafast green microwave-assisted synthesis of high-entropy oxide nanoparticles for Li-ion battery applications. *Mater Chem Phys.* 2021;262:124265. doi:10.1016/j.matchemphys.2021.124265
  37. Li Z, Chen H, Liu WJC. Full-spectrum photocatalytic activity of ZnO/CuO/ZnFe<sub>2</sub>O<sub>4</sub> nanocomposite as a photofenton-like catalyst. *Catalysts.* 2018;8(11):557.
  38. Chen L, Wang Y, Yu F, Shen X, Duan C. A simple strategy for engineering heterostructures of Au nanoparticle-loaded metal-organic framework nanosheets to achieve plasmon-enhanced photocatalytic CO<sub>2</sub> conversion under visible light. *J Mater Chem A.* 2019;7(18):11355-11361.
  39. Yu C, Wang Y, Zhang J, et al. Integration of mesoporous nickel cobalt oxide nanosheets with ultrathin layer carbon wrapped TiO<sub>2</sub> nanotube arrays for high-performance supercapacitors. *New J Chem.* 2016;40(8):6881-6889. doi:10.1039/C6NJ00359A
  40. Sun Z, Zhang J, Yin L, et al. Conductive porous vanadium nitride/graphene composite as chemical anchor of polysulfides for lithium-sulfur batteries. *Nat Commun.* 2017;8(1):14627.
  41. Chen R, Zhao T, Wu F. From a historic review to horizons beyond: lithium-sulphur batteries run on the wheels. *Chem Commun.* 2015;51(1):18-33.
  42. Song Y, Zhao W, Zhu X, et al. Vanadium dioxide-graphene composite with ultrafast anchoring behavior of polysulfides for lithium-sulfur batteries. *ACS Appl Mater Interf.* 2018;10(18):15733-15741.
  43. Razaq R, Sun D, Xin Y, et al. Nanoparticle Assembled Mesoporous MoO<sub>2</sub> Microrods Derived from Metal Organic Framework and Wrapped with Graphene as the Sulfur Host for Long-Life Lithium-Sulfur Batteries. *Adv Mater Interf.* 2019;6(4):1801636.
  44. Elazari R, Salitra G, Garsuch A, Panchenko A. Sulfur-impregnated activated carbon fiber cloth as a binder-free cathode for rechargeable Li-S batteries. *D Aurbach.* 2011;23(47):5641-5644. doi:10.1002/adma.201103274
  45. Knap V, Stroe DI, Swierczynski M, Teodorescu R, Schaltz E. Investigation of the self-discharge behavior of lithium-sulfur batteries. *J Electrochem Soc.* 2016;163(6):A911-A916. doi:10.1149/2.0641606jes
  46. Lin H, Yang L, Jiang X, et al. Electrocatalysis of polysulfide conversion by sulfur-deficient MoS<sub>2</sub> nanoflakes for lithium-sulfur batteries. *Energ Environ Sci.* 2017;10(6):1476-1486. doi:10.1039/C7EE01047H



47. Pitale SS, Nagpure IM, Kumar V, Ntwaeaborwa OM, Terblans JJ, Swart HC. Investigations on the low voltage cathodoluminescence stability and surface chemical behaviour using auger and X-ray photoelectron spectroscopy on LiSrBO<sub>3</sub>:Sm<sup>3+</sup>+phosphor. *Mater Res Bull.* 2011;46(7):987-994. doi:[10.1016/j.materresbull.2011.03.022](https://doi.org/10.1016/j.materresbull.2011.03.022)
48. Yao KPC, Kwabi DG, Quinlan RA, et al. Thermal stability of Li<sub>2</sub>O<sub>2</sub> and Li<sub>2</sub>O for Li-air batteries: In situ XRD and XPS studies. *J Electrochem Soc.* 2013;160(6):A824-A831. doi:[10.1149/2.069306jes](https://doi.org/10.1149/2.069306jes)
49. Rangel R, Bartolo-Pérez P, Martínez E, Trejo-Cruz XA, Díaz G, Galván DH. Catalytic activity and X-ray photoelectron spectroscopy performance of Bi<sub>2</sub>MoxW(1-x)O<sub>6</sub> solid-solutions. *Cat Sci Technol.* 2012;2(4):847-852. doi:[10.1039/c2cy00506a](https://doi.org/10.1039/c2cy00506a)

## SUPPORTING INFORMATION

Additional supporting information can be found online in the Supporting Information section at the end of this article.

**How to cite this article:** Raza H, Cheng J, Lin C, Majumder S, Zheng G, Chen G. High-entropy stabilized oxides derived via a low-temperature template route for high-performance lithium-sulfur batteries. *EcoMat.* 2023;5(4):e12324. doi:[10.1002/eom2.12324](https://doi.org/10.1002/eom2.12324)